Small

NANO · MICRO small
www.small-journal.com

RESEARCH ARTICLE

Skin-Conformal Thermo-Haptic Interface With Advanced Thermal Management for Multimodal Haptic Feedback

Su Li[1] | Si Chen[1] | Samantha Zborovsky[1] | Ziran Du[1] | Yizong Li[1] | Penghao Dong[1] | Kaiyan Qiu[2] | Shanshan Yao[1]

[1]Department of Mechanical Engineering, Stony Brook University, Stony Brook, New York, USA | [2]School of Mechanical and Materials Engineering, Washington State University, Pullman, Washington, USA

Correspondence: Shanshan Yao (shanshan.yao@stonybrook.edu)

Received: 21 April 2026 | **Revised:** 29 July 2026 | **Accepted:** 19 August 2026

Keywords: electromagnetic actuators | heat sinks | heating/cooling devices | multimodal haptic interfaces | phase change materials | thermal interfaces | thermoelectric devices

ABSTRACT

Tactile perception arises from coordinated activation of mechanoreceptors and thermoreceptors, yet most wearable haptic technologies primarily stimulate mechanoreceptors. Thermal haptic interfaces remain constrained by rigid heat sinks, unstable hydrogels, or insufficient thermal management; thus compact integration of active thermal and mechanical actuation in a skin-conformable platform remains difficult. Here, we present a compliant thermal haptic device that enables bidirectional heating and cooling without rigid heat dissipation structures. The device uses a polymer matrix filled with hexagonal boron nitride and phase-change materials to form dynamic, effective thermal pathways. A soft heat sink based on gallium-polymer composites provides stable thermal regulation while preserving compliance. A gallium-based soft electromagnetic actuator is further integrated for mechanical haptic feedback. The thermo- and mechano-haptic components are connected through a kirigami-inspired architecture, enabling simultaneous mechanical and thermal feedback in a stretchable platform. Preliminary user tests show that multimodal feedback improves material-recognition accuracy to 96.4%, compared with 74.9% for mechanical-only cues and 87.6% for thermal-only cues. These results offer materials and integration strategies for skin-integrated multimodal haptics, with potential applications in VR/AR, telepresence, prosthetics, and rehabilitation.

1 | Introduction

Tactile perception, enabled by the co-activation of mechanoreceptors and thermoreceptors in the skin, is essential for the body to sense its surroundings [1–4]. Most current wearable haptic technologies focus on mechanoreceptive stimulation, using external force [5–7], vibration [8], or electrical impulses [9] to stimulate touch. Despite the great progress in mechano-haptic devices, thermo-haptic interfaces and multimodal haptic systems that can match the skin's mechanical and tactile perception capabilities remain largely unexplored [10, 11]. However, thermal cues play a vital role in environmental interaction. Thermoreceptors convert rapid temperature transients into neural signals with high sensitivity across a broad range, capturing realistic thermal information that robustly enriches human perception [1, 12]. Importantly, human skin can perceive temperature changes within approximately 15°C–45°C without pain or tissue damage [12]. Everyday experiences, for instance, touching cold bottles or hot mugs, or transitioning from outdoor cold to indoor warmth in winter, impose distinct heat-flux profiles on the skin due to the various thermal properties of different objects or environments [13]. These spatial-thermal heat flows are instantly encoded by thermoreceptors, enabling reliable perception of objects and environmental conditions. Therefore, developing skin-compatible thermal haptic devices and integrating thermal and mechanical interfaces within a single conformal platform are essential for achieving accurate and realistic haptic feedback.

This need is also supported by prior haptic perception studies, which show that mechanical and thermal cues provide complementary information for material recognition (Table S1). Mechanical haptic interfaces can render stiffness, texture, and shape, but mechanical feedback alone can be ambiguous for materials with similar compliance but different thermal properties [5–10, 14]. Similarly, thermal haptic interfaces provide heat-flux cues related to material thermal properties, but thermal-only feedback can also leave ambiguity between materials with similar thermal responses [12, 15]. Existing multimodal systems combining thermal and mechanical cues have improved material or object discrimination compared with single-modality feedback [11, 16]. These findings motivate the development of a compliant platform that can deliver co-located thermal and mechanical cues.

Translating this perceptual motivation into a skin-soft device remains challenging, especially for bidirectional heating and cooling. Cooling is intrinsically more difficult than heating, given that baseline skin temperature typically exceeds room temperature. Early implementations predominantly focused on achieving a relatively simple heating function based on Joule heating [15–22]. While these devices offer mechanical flexibility, they can only render a limited portion of the perceptual temperature spectrum and cannot emulate the thermal profiles of objects cooler than the skin temperature. Consequently, thermoelectric devices based on the Peltier effect have been explored for bidirectional thermal actuation, but several challenges remain. On one hand, the performance of the thermal interface materials (TIMs) between the skin and thermoelectric elements remains a primary limitation. TIMs are critical components designed to improve interfacial thermal transfer and provide mechanical support [23–25]. To improve mechanical compliance, some studies have explored stretchable thermal interfaces by incorporating high thermal conductivity fillers into a skin-like polymer matrix [12, 16, 20, 26–31]. However, high loading ratios of rigid fillers (e.g., ceramics, carbon materials) severely compromise mechanical compliance, leading to a degradation of stretchability [32]. Fabrication methods designed to create 3D conductive networks, such as ice templating or chemical vapor deposition, are often complex and difficult to scale for practical manufacturing [33–35].

On the other hand, effective bidirectional thermal actuation relies on heat sinks to continuously dissipate heat from the hot side and maintain a stable temperature gradient across the module, thereby preventing thermal saturation during thermoelectric operation [36, 37]. In most reported systems, this function is achieved by using rigid, bulky components, such as commercial copper or aluminum fin structures, which significantly compromise device stretchability and skin conformability [12, 24, 38, 39]. Additionally, microscopic air gaps between rigid heat sinks and the nonplanar skin surface increase parasitic contact thermal resistance and reduce the effective temperature delivered to the skin [40]. Soft heat sink alternatives remain limited. For example, Wang et al. demonstrated a cooling hydrogel that serves as an effective heat sink while maintaining softness [15]. However, evaporation-induced water loss can cause performance drift and limit long-term operation.

Finally, integrating bidirectional thermo-haptic modules with mechano-haptic ones into a single skin-integrated haptic system is necessary to elicit skin responses from both mechanoreceptors and thermoreceptors. Mechanical compliance is essential for the fidelity of haptic information transfer at the epidermis, given the soft, stretchable, curvilinear nature of human skin [12, 41–43]. Conventional rigid devices fail to establish conformal contact with the skin's surface, resulting in a limited effective contact area that impedes mechanical and thermal transfer between the device and the skin [44].

Here, we present the design, fabrication, and characterization of a soft thermal haptic interface and integrated multimodal haptic interface (Figure 1). As shown in Figure 1a, the multimodal haptic device (Figure 1b) delivers concurrent mechanical (vibration) and thermal (warm and cold) stimuli, which are processed by the user's somatosensory system. The thermal subsystem (i.e., thermo-haptic unit) is engineered for rapid transient operation and relies on the Peltier effect for bidirectional thermal modulation [45]. To enhance thermal transfer while preserving compliance, the subsystem incorporates a polydimethylsiloxane (PDMS) matrix with hexagonal boron nitride (h-BN) fillers to improve heat conduction and paraffin as a phase-change material (PCM) to create dynamic thermal pathways. In addition, a flexible gallium (Ga)/PDMS heat sink is designed to dissipate heat from the hot side, suppress thermal backflow, and maintain the required temperature gradient even under deformation. The mechanical subsystem (i.e., mechano-haptic unit) employs electromagnetic actuation using a Ga coil, preserving stretchability while delivering repeatable vibrational cues.

The two subsystems are integrated through a kirigami element, which mechanically and electrically bridges the thermal and mechanical subsystems, maintains reversible stretchability, and ensures intimate contact with the epidermis. The operating principle illustrated in Figure 1c shows simultaneous stimulation of cutaneous thermoreceptors and mechanoreceptors, allowing users to perceive complex, multimodal sensations and to discriminate representative materials (aluminum, glass, polypropylene (PP), printing paper, and PDMS). In user studies, the platform improves object-recognition accuracy from 74.9% with mechanical-only feedback and 87.6% with thermal-only feedback to 96.4% with multimodal feedback.

Our device addresses current multimodal haptic gaps (Table S2) through the following core advancements: (1) Previously reported bidirectional thermo-haptic interfaces typically rely on rigid heat sinks or environmentally sensitive hydrogels. Our compliant heat sink ensures the mechanical compliance of the entire thermo-haptic system while maintaining effective thermal dissipation; (2) Current fully compliant thermo-haptic devices are mostly based on Joule heating and limited to heating only, our platform enables both active heating and cooling in a skin-conformable platform; (3) While existing research either demonstrates soft mechanical interfaces alone or multimodal designs limited by rigid heat sinks, our platform represents a rare (if not unique) solution capable of providing simultaneous, bidirectional thermal and mechanical feedback within a fully skin-conformable, stretchable

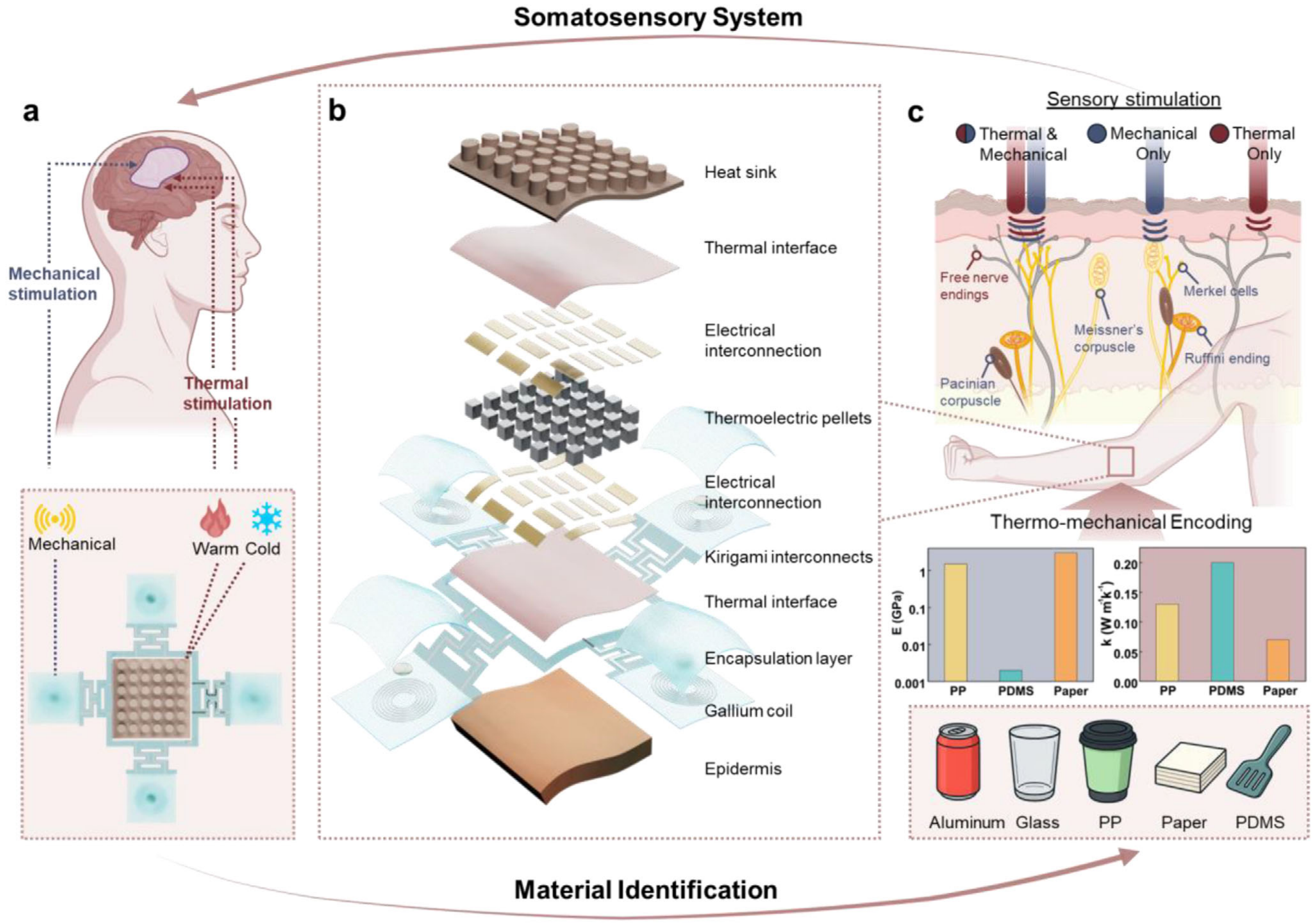

FIGURE 1 | Design and operation of a skin-integrated multimodal haptic device. (a) Conceptual illustration of the haptic system for both mechanical and thermal stimulation. (b) Exploded-view schematics of the device's multilayer architecture. (c) Illustration of the multimodal skin haptic stimulation. As an example, for virtual material discrimination, the device generates distinct thermal and mechanical haptic stimulation relevant to materials' thermal and mechanical properties. The corresponding haptic stimulation activates cutaneous thermoreceptors and mechanoreceptors to render distinct thermal and mechanical sensations on the skin for material discrimination.

architecture; and (4) the preliminary material-recognition study shows that combined thermal and mechanical cues reduce ambiguity that remains under either single-modality condition.

2 | Results and Discussion

2.1 | Overview of the Thermoelectric Module

To realize a skin-compatible heating/cooling haptic interface, a stretchable thermoelectric module (TEM) capable of rapid, bidirectional thermal actuation is developed. The module's performance is governed by three primary components: (1) semiconductor thermoelectric pellets (Bi_2Te_3 in this work) that generate the thermal flux, (2) substrates (thermal interfaces on the skin side and exposed to the surroundings) that conduct heat and provide mechanical integrity, and (3) a heat sink that dissipates heat from the hot side and maintains the temperature gradient required for stable thermoelectric operation.

Figure 2a presents the schematic of the TEM. Figure 2b,c illustrates the working principle of the TEM for heating and cooling. The bidirectional operation is controlled by the direction of the applied current [45]. For the heating mode (Figure 2b), an applied current causes charge carriers (electrons in n-type, holes in p-type) to move downward. This net carrier transport pumps heat from the top side (air-exposed) to the bottom side (skin-facing). Consequently, the bottom surface has a higher temperature T_{hot}, delivering warm sensations. Conversely, the reversing current switches the module to cooling mode (Figure 2c). Heat is pumped away from the bottom side (skin-facing) toward the top side as the net carriers move upward, resulting in a lower temperature T_{cold} with cold sensations.

2.2 | Compliant and Efficient Thermal Interface

While thermoelectric pellets enable controllable temperature inversion, achieving a significant temperature difference (ΔT) between their active (skin-facing) and dissipation (air-exposed) surfaces is crucial. A larger ΔT establishes a steeper temperature gradient, which increases the heat flux delivered from the active surface through the TIM to the epidermis and enhances thermal perception [46]. Translating this internal temperature gradient into effective tactile feedback relies heavily on the module's substrate (TIMs). TIMs should combine high thermal

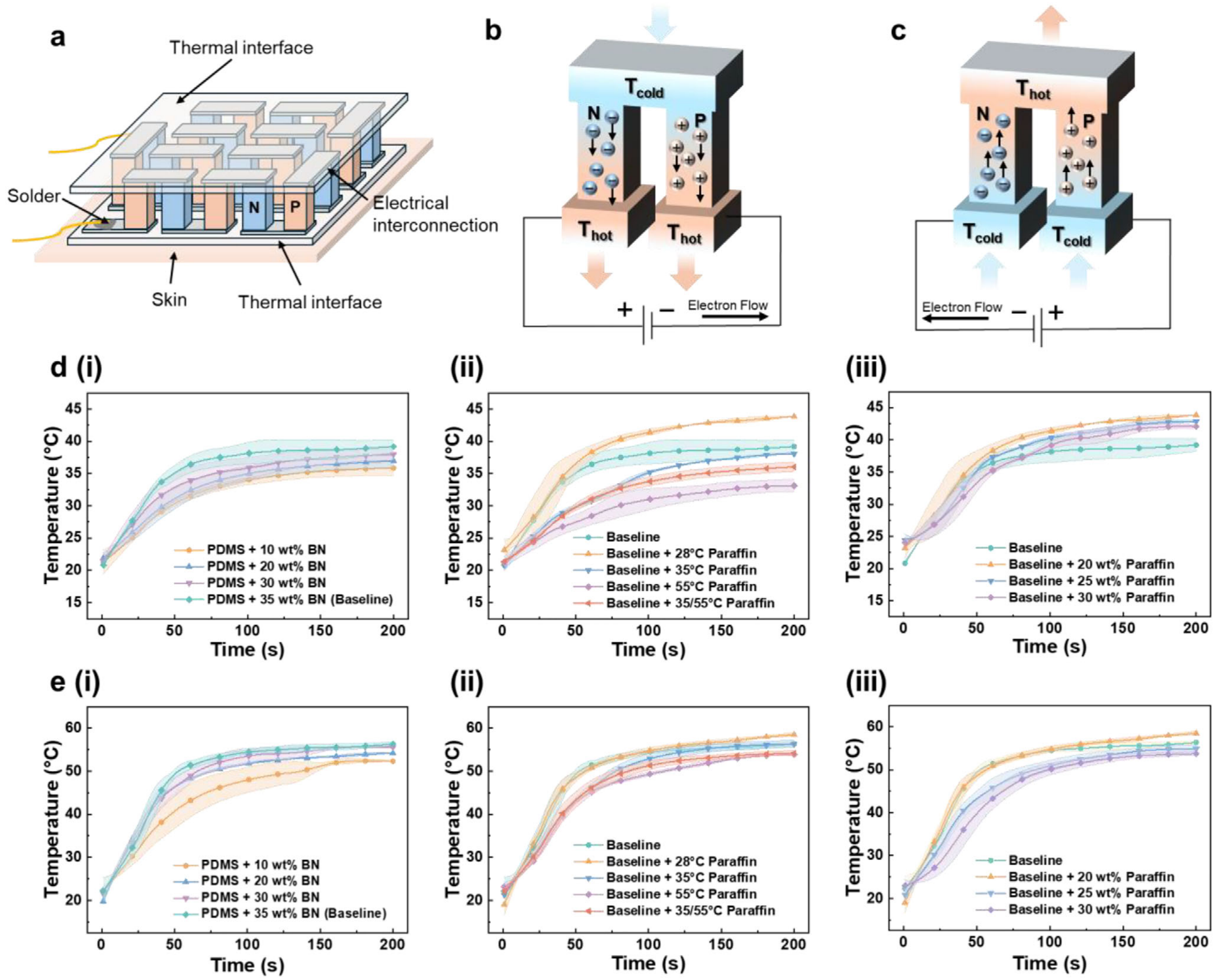

FIGURE 2 | Thermoelectric mechanism and TIM optimization. (a) Schematic of the overall structure of the TIM. (b) Heating-mode mechanism. (c) Cooling-mode mechanism. Temperature profiles measured (d) at the skin-facing TIM in the skin heating mode and (e) at the air-exposed TIM in the skin cooling mode: (i) PDMS composites with h-BN loadings of 10, 20, 30, 35 wt.%. The PDMS with 35 wt.% h-BN composite is denoted as the "Baseline" for subsequent experiments. (ii) Baseline matrix loaded with paraffin of different melting points (28°C, 35°C, 55°C, and a 1:1 (w/w) mixture of 35/55°C), all at a 20 wt.% loading (relative to PDMS). (iii) Baseline matrix with various loadings (20, 25, 30 wt.%) of the 28°C paraffin.

conductivity and mechanical compliance to minimize interfacial thermal resistance while maintaining conformal contact with the curvilinear skin surface. In addition, the skin-facing TIM acts as a soft heat spreader, ensuring the user perceives a uniform temperature and mitigating local hot or cold spots. Commercial modules commonly use a rigid ceramic substrate, such as alumina, due to its relatively high thermal conductivity [47]. However, imperfect contact between rigid substrates and soft skin can introduce substantial contact thermal resistance, limiting heat transfer to the epidermis.

In this work, the TIMs employ PDMS as a compliant matrix and incorporate h-BN fillers with a biocompatible organic paraffin to enhance effective thermal transport while preserving mechanical compliance. The choice of h-BN is motivated by its chemically stable, graphite-like lamellar structure and pronounced thermal anisotropy (in-plane ≈ 250–400 $W \cdot m^{-1} \cdot K^{-1}$; through-plane ≈ 2–10 $W \cdot m^{-1} \cdot K^{-1}$) [48]. In this composite TIM, h-BN primarily promotes lateral heat spreading to improve temperature uniformity across the contact area. Heat transfer in the thickness direction is more sensitive to interfacial resistance and microstructural discontinuities. Paraffin can further improve transient thermal response through two complementary mechanisms. First, upon heating, paraffin transitions to a liquid state; this molten-phase conduction can infiltrate microvoids and bridge interfaces between h-BN platelet structures and the PDMS matrix, reducing interfacial thermal resistance and improving heat transport in the through-thickness direction [49–51]. Second, the melting and crystallization of paraffin provide latent heat storage that increases the effective heat capacity of the composite. This thermal buffering reduces temperature overshoot and stabilizes temperature evolution during both heating and cooling [52, 53].

The thermal performance of the developed TIMs was evaluated for heat transfer between TE pellets and the skin-facing interface (Figure 2d) as well as heat dissipation through the air-exposed interface (Figure 2e). In the skin heating mode, the temperature evolution of the skin-facing TIM was recorded starting from room temperature (Figure 2d). In the skin cooling mode, heat extracted from the skin is transported to the TIM on the hot side of the TEM and must be dissipated to the ambient to sustain cooling. We therefore monitored the temperature rise of the air-exposed TIM as an indicator of heat dissipation capability (Figure 2e). Figure 2d,i; Figure 2e,i compare h-BN/PDMS composites containing different loadings of h-BN fillers as the skin-facing and air-exposed TIMs, respectively. For both TIMs, increasing the h-BN loading results in a faster rate of temperature increase and higher steady temperatures, consistent with enhanced thermal transport through the composites. Based on these trends, the 35 wt.% h-BN/PDMS composite was selected as the baseline formulation to incorporate paraffin.

Paraffins with different melting points (28°C, 35°C, and 55°C) were then introduced into the 35 wt.% h-BN/PDMS matrix at a fixed loading of 20 wt.% relative to PDMS. A 1:1 (w/w) mixture of 35°C and 55°C was also evaluated to broaden the transition window. For the skin-facing TIM (Figure 2d,ii), the composite containing 28°C paraffin exhibits a faster thermal transient and a higher steady-state temperature, indicating improved heat delivery to the skin-facing interface. For the air-exposed TIM (Figure 2e,ii), the composite containing 28°C paraffin formulation initially shows a temperature trajectory comparable to the 35 wt.% h-BN/PDMS baseline. This behavior is consistent with the solid-liquid phase transition of paraffin, during which latent heat absorption increases the effective heat capacity of the composite and temporarily buffers the temperature increase [48]. As the transition progresses, the molten-phase paraffin bridges microgaps within the composite to form conductive pathways and reduce interfacial thermal resistance. After the phase transition is complete, conductive transport is dominant and the 28°C paraffin composite exhibits a higher temperature rise than the 35 wt.% h-BN/PDMS baseline.

Based on the improved thermal response on both the skin-facing and air-exposed sides, paraffin with a melting point of 28°C was selected as a secondary filler for both TIMs. To balance conductive transport and phase-transition buffering, we further evaluated 28°C paraffin loadings of 20, 25, and 30 wt.% (Figure 2d,iii;e,iii). A loading of 20 wt.% provides a practical optimum that results in fast and effective thermal response due to the balanced thermal transport and transient buffering associated with latent heat. The measured steady-state through-plane thermal conductivities of the PDMS-based composites, including the h-BN/PDMS loading series and the optimized 28°C paraffin-containing TIM formulation, are summarized in Table S3. These values mainly reflect near-room-temperature through-plane conductive transport under a small temperature gradient and should be distinguished from the transient thermal response of the TIM during device operation. Although the optimized 28°C paraffin-containing TIM shows a slightly lower steady-state thermal conductivity than 35 wt.% h-BN/PDMS, this decrease is mainly attributed to the compositional change after paraffin addition, which increases the non-BN fraction and can partially dilute the h-BN conductive network. During operation, its solid-liquid phase transition provides latent-heat buffering, which helps moderate temperature evolution and reduce overshoot. After melting, paraffin also improves local interfacial contact by filling microvoids and bridging discontinuities between h-BN platelets and the PDMS matrix. Thus, the optimized BN/paraffin/PDMS composite functions as a thermal interface material for improving interfacial heat transfer and transient thermal regulation at the module interfaces. However, continuous heat dissipation from the hot side of the thermoelectric module requires a separate soft heat-sink structure with high effective thermal conduction and enlarged convective surface area. If the BN/paraffin/PDMS composite were used as the heat-sink material, the paraffin phase would mainly provide transient heat absorption during melting rather than sustained heat rejection to the ambient environment. In addition, the TIM layer does not provide the three-dimensional geometry needed to enlarge the convective heat-transfer area. Therefore, the BN/paraffin/PDMS TIM and the Ga/PDMS heat sink are complementary rather than interchangeable.

2.3 | Soft Ga/PDMS Heat Sink

To address the constraints posed by existing rigid heat sinks, we explored the Ga/polymer composite to develop a flexible heat sink that combines high effective thermal transport with mechanical compliance under deformation [54–56]. Owing to Ga's low liquid phase transition temperature of 29.8°C and high thermal conductivity of 40 $W·m^{-1}·K^{-1}$ [57, 58], the liquid metal phase forms effective, reconfigurable thermal pathways within an elastomer matrix, enabling deformable heat dissipation suitable for wearable platforms. Because pure Ga has a phase-transition temperature close to room temperature, we considered its phase state during thermal operation. During skin cooling operation, heat extracted from the skin-facing interface is transported toward the heat-sink side and dissipated to the ambient environment. During skin-heating operation, the opposite side of the thermoelectric module, where the Ga/PDMS heat sink is located, can remain near room temperature or fall below the melting point of pure Ga. Therefore, we do not assume that Ga remains fully liquid under all operating conditions. However, the macroscopic deformability of the heat sink is mainly governed by the PDMS matrix and the compliant pin-fin architecture, with Ga embedded within the elastomer matrix. Experimentally (Figure S1), the Ga/PDMS heat-sink side remained within 21.9°C–23.5°C during skin-heating operation, while the skin-heating side increased to 45°C. This heat-sink-side temperature range is below the melting point of pure Ga, indicating that possible local Ga solidification may occur under this condition. Nevertheless, experimental results (Figure S1) show that show that the Ga/PDMS heat sink remains readily deformable under stretching, bending, and twisting, without visible cracking, delamination, or leakage. These results indicate that the macroscopic compliance of the soft heat sink is maintained even when the heat-sink side operates below the melting point of pure Ga.

Based on this material and structural design, the soft heat sink was fabricated via a multi-step molding and demolding process as shown in Figure 3a and Figure S2, with details given in the Experimental Section. Ga/PDMS heat sink with a pin-fin array was optimized by evaluating fin efficiency η_{fa} and thermal resistance R_{fa} as functions of the pin-fin parameters. The analysis follows the classical one-dimensional constant cross-section pin-fin model. The array metrics are calculated in three stages: (i) obtain the single fin efficiency η_f; (ii) determine the effective heat

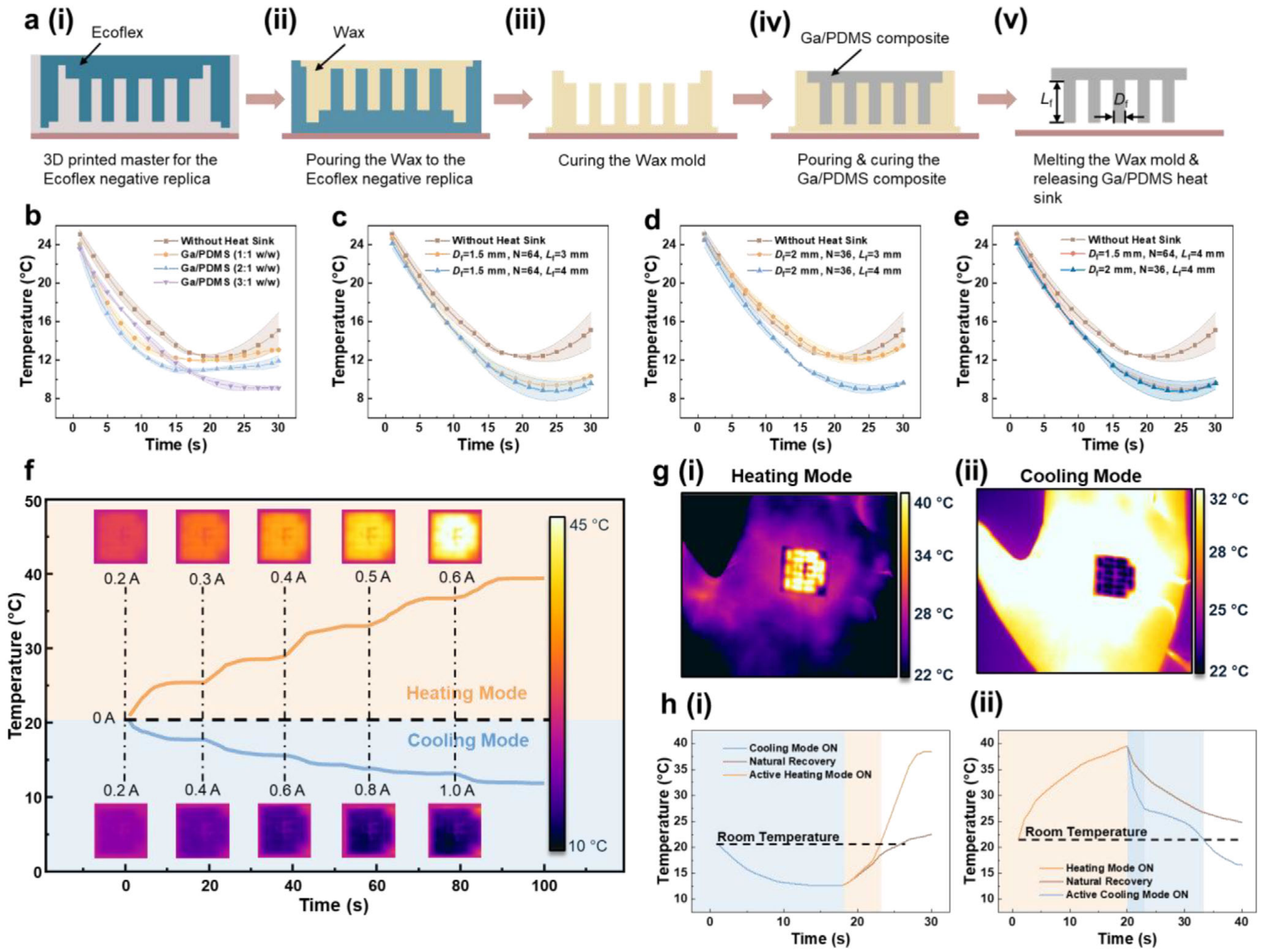

FIGURE 3 | Design, fabrication, and thermal performance optimization of the TEM. (a) Schematics of the heat sink fabrication processes. (b) Cooling mode response of the TE module with heat sinks at different Ga/PDMS weight ratios and without a heat sink. Cooling performance of TE modules with varying heat sink pin lengths at (c) high and (d) low array densities. (e) Cooling mode response of the TEM with Ga/PDMS heat sinks at different array densities and lengths. The Ga/PDMS weight ratio in (c) to (e) was maintained at 3:1. (f) Time-resolved temperature profiles and corresponding IR camera images with the stepwise current increase, in both heating and cooling modes. The ambient temperature is indicated by the dashed horizontal line. The drive current was stepped at 20 s intervals within the skin-comfortable window. (g) In situ IR thermographs of a 20 mm × 20 mm TEM laminated on the palm: (i) heating mode; (ii) cooling mode. (h) Comparisons between the active temperature recovery and passive natural recovery to room temperature after turning off current: (i) recovery after cooling; (ii) recovery after heating. Cooling and heating modes operate at currents of 0.8 and 0.6 A, respectively.

-exchange areas from the array geometry; and (iii) combine them to yield the array fin efficiency η_{fa} and thermal resistance R_{fa}. Detailed derivations are provided in Note S1. Finally, the array fin efficiency η_{fa} and the convective thermal resistance R_{fa} are obtained as:

$$\eta_{fa} = 1 - \frac{A_f}{A_t}(1 - \eta_f),\ R_{fa} = \frac{1}{hA_f} \quad (1)$$

where A_f is the lateral fin area, A_t is the total effective heat exchange area, and h is the convective heat-transfer coefficient.

Table 1 summarizes the geometric parameters and the corresponding computed metrics obtained from Equation (1). To validate these predictions, a TEM operating in cooling mode from ambient temperature was tested. Figure 3b shows that increasing the Ga weight ratio in Ga/PDMS (from 1:1 to 3:1) results in a faster decrease in surface temperature and a lower terminal temperature. This trend is consistent with the increased effective thermal conductivity k_f with higher Ga loading ratios, which enhances internal heat spreading and reduces the overall thermal resistance for heat removal. According to the classical pin-fin analysis [46], a higher fin thermal conductivity k increases fin efficiency η_f (Equation S2 and Equation S3), and a longer pin length L_f reduces the effective convective thermal resistance of the pin-fin array R_{fa} (Equation 1 and Note S1), thus accelerating the decrease in surface temperature.

Figure 3c,d examine the pin length at two array densities. At higher array density (Figure 3c), extending the pin length from $L_f = 3$ to 4 mm increases the corrected fin length L_c and lateral area A_f (Equations S1 and S4). Consistent with Table 1, this causes a modest drop in η_{fa} from 89.8% to 83.6%, but a large reduction in R_{fa} from 85.4 to 74.4 K W^{-1}. The two designs

TABLE 1 | Pin-fin geometry and predicted fin-array efficiency and thermal resistance.

Diameter D (mm)	Fin length L_f (mm)	Number of pins N	Array pin efficiency η_{fa} (%)	Convective thermal resistance R_{fa} (K W^{-1})
1.5	4	$8 \times 8 = 64$	83.6	74.4
1.5	3	$8 \times 8 = 64$	89.8	85.4
2.0	4	$6 \times 6 = 36$	87.0	88.4
2.0	3	$6 \times 6 = 36$	92.0	100.8

exhibit similar cooling profiles in the initial 15 s. Beyond 15s, the longer pins cool faster and reach a lower plateau. The same trend is observed at lower density (Figure 3d). Notably, the lower density design ($L_f = 3$ mm) exhibits a relatively high R_{fa}, so its cooling advantage over the bare TE module is limited. Figure 3e compares the two $L_f = 4$ mm designs. The smaller diameter, higher-density array ($D = 1.5$ mm, $N = 64$) and the larger diameter, lower-density array ($D = 2$ mm, $N = 36$) exhibit similar thermal profiles. Considering thermal performance with the overall device footprint and fabrication complexity for the skin-integrated system, we adopt $D = 2$ mm, $N = 36$, $L_f = 4$ mm as the optimized design. The comparison between the fabricated soft Ga/PDMS heat sink and a commercial copper heat sink is shown in Figure S3. During thermoelectric heating, the soft Ga/PDMS heat sink more effectively suppressed the temperature rise on the heat-sink side of the module, indicating improved heat dissipation under the tested configuration. Unlike the rigid copper heat sink, the soft Ga/PDMS heat sink also preserves mechanical deformability, supporting its use in skin-conformal thermo-haptic platforms.

2.4 | Performance of Integrated Thermoelectric Module

The optimized TIMs and Ga/PDMS heat sink were integrated with the Bi_2Te_3 thermoelectric pellet (1.4 mm × 1.4 mm × 1.7 mm) array and flexible silver electrodes to form the TEM (Figure S4 and Experimental Section). Time-resolved temperature profiles for both cooling and heating modes were recorded at the skin-facing TIM surface, accompanied by IR thermography sampled at varied currents (Figure 3f). Temperature curves demonstrate that the TEM rapidly delivers heating and cooling to the skin, with the attainable temperature level managed by the applied current. The integrated TEM, with soft TIMs, a soft heat sink, and flexible interconnection, is able to be laminated onto soft, curved human body regions. Figure 3g shows in situ IR thermographs of a TEM mounted on the palm (as a representative curved surface). Both modes deliver thermal profiles sufficient to evoke clear warm and cold sensations, making the developed TEM compatible with on-skin haptic feedback.

Critically, the bidirectional Peltier operation enables the TEM to actively return to baseline by reversing the current direction. Figure 3h compares the temperature recovery to room temperature after cooling (Figure 3h,i) and heating (Figure3h, ii) based on passive recovery (natural convection) and active recovery (enabled by reversing the current direction). In both cooling and heating modes, the recovery time is much shorter than that under passive recovery. The skin temperature management is additionally assisted by the paraffin. When skin heating is engaged, the paraffin in the skin-facing TIM melts and establishes thermal pathways to facilitate heat transfer to the skin. Its solid-liquid phase-change absorbs excess heat as latent-heat buffering, thereby preventing temperature overshoot and enhancing safety. During cooling, the paraffin, which stores latent heat during the preceding heating process, solidifies and releases latent heat. The active temperature recovery accelerates the slower, environment-dependent recovery associated with passive natural convection, which is essential for real-time haptic feedback.

2.5 | Integration of Thermal and Mechanical Haptic Modalities

2.5.1 | Gallium-Based Electromagnetic Actuator for Mechano-Haptic Feedback

The reported thermo-haptic interface is further integrated with a mechano-haptic interface to provide mechanical tactile representation. The core is an electromagnetic actuator that generates skin deformation based on the Lorentz force. Specifically, the actuator consists of a Ga liquid-metal coil and a permanent magnet suspended on top of the coil. Ga is employed as the stretchable conductor for the coil and interconnection (discussed later) materials due to its exceptional electrical conductivity and high mechanical compliance at skin temperature (solid-liquid transition temperature of 29.8°C) [59]. When a current flows through the coil, the interaction between the magnetic field generated by the current-carrying coil and the permanent magnet produces a force that drives out-of-plane motion of the magnet, thereby delivering vibrotactile cues with tunable amplitude [60]. To ensure consistent performance and conformal contact with the skin, the Ga coil is encapsulated in an Ecoflex layer. The fabricated Ga coil exhibits uniform trace width and turn spacing (Figure 4a). Figure S5 confirms that the magnetic flux density of the coil increases approximately linearly with the applied current, allowing for tunable amplitudes of the electromagnetic actuator.

Because the mechanical actuator is co-located with the thermal haptic module on the skin, Joule heating in the coil should be minimized to avoid confounding thermal perception, and the local temperature should remain below 45°C to prevent triggering the skin's pain receptors [14]. The coil temperature increases with increasing applied current (Figure 4b), with a steeper rise at higher currents. Based on this current-temperature relationship, we selected 1.0 A as the operating current, at which the coil temperature of 34.5°C remains close to typical skin temperature.

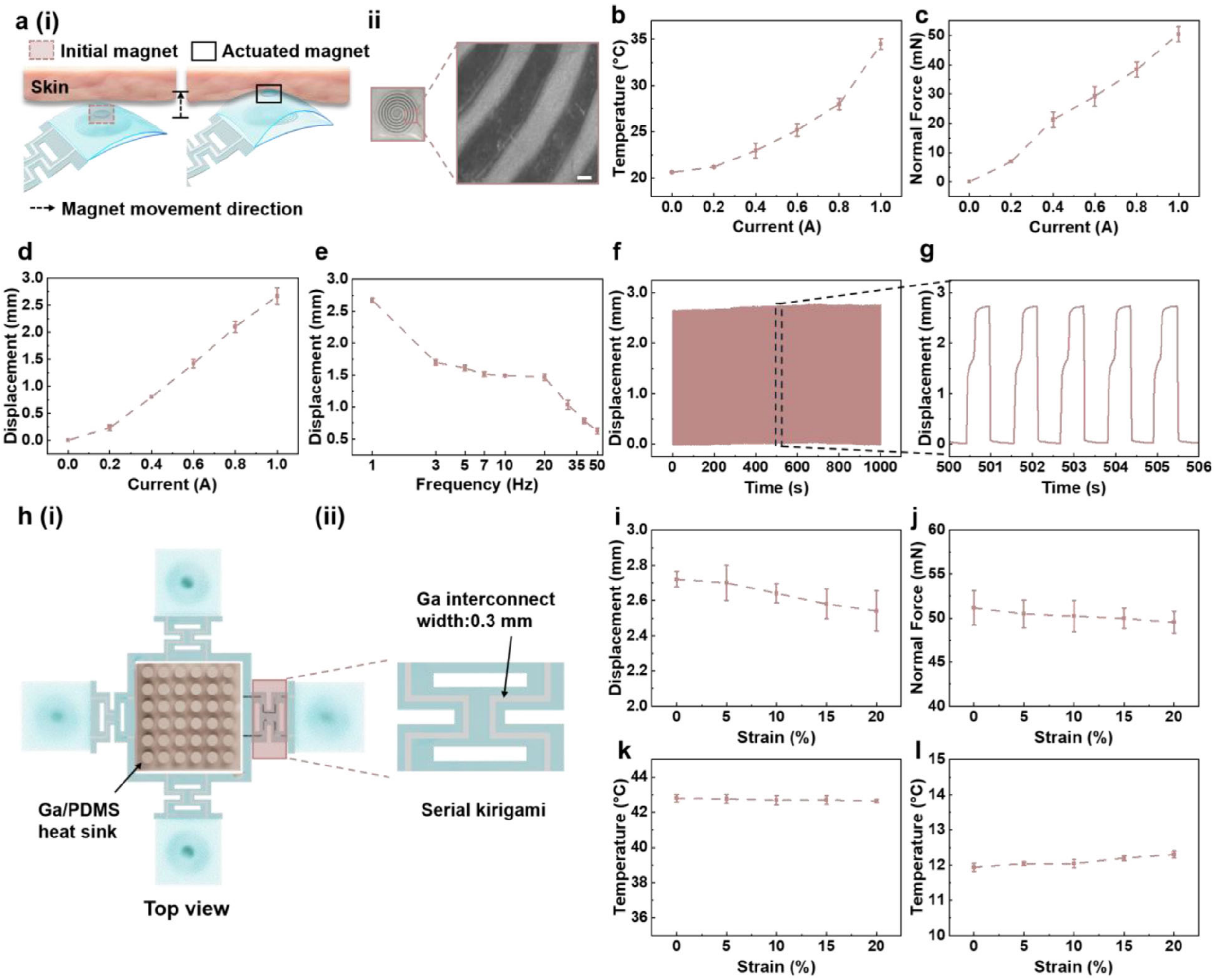

FIGURE 4 | Performance of the electromagnetic mechano-haptic actuator and integrated multimodal haptic device. (a) Actuator design and principle: (i) Schematic illustrating the vibrotactile operation, where the Ga coil drives an actuated magnet to indent the skin. (ii) Microscopic image of the printed coil traces. Scale bar, 200 µm. (b) Coil temperature, (c) generated normal force, and (d) generated out-of-plane displacement of the actuator as a function of applied current. (e) Frequency response of the actuator displacement. (f,g) Cycling stability test over 1,000 actuation cycles. (h) Top view schematic of the multimodal haptic device. (i) Displacement and (j) normal force generated by the actuator under different strains. (k) Heating (0.6 A) and (l) cooling (1.0 A) performance of the thermal unit under different strains. All measurements in (e,f,i,j) were performed with a coil current of 1.0 A.

Figures S6 and S7 demonstrate the electromechanical robustness of the coil. The coil maintains a stable resistance (~ 0.8 Ω) across the phase transition. When attached to the skin surface, the Ga coil maintains a liquid phase that can sustain tensile strain up to 120%, without structural failure and a significant increase in electrical resistance. The good stretchability ensures reproducible magnetic output and haptic actuation.

For mechanical haptic actuators, perceptual thresholds for normal indentation are around 100 µm displacement and 15 mN force [61]. The normal force increases approximately linearly with current (Figure 4c), reaching approximately 22 mN at 0.4 A and 50 mN at 1.0 A, both exceeding the reported perceptual threshold. The out-of-plane displacement also increases with current (Figure 4d) and reaches around 2.7 mm at 1.0 A, providing sufficient indentation amplitude for clearly perceptible tactile cues. The frequency response (Figure 4e) shows that the displacement amplitude decreases with increasing frequency. Finally, cyclic testing over 1,000 actuation cycles (Figure 4f,g) verifies stable actuation with no observable degradation, indicating robust electromechanical reliability under repeated operation. These results demonstrate that the electromagnetic actuator is able to deliver strong, controllable, and durable mechanical stimuli compatible with skin-integrated haptic systems.

2.5.2 | Gallium-Filled Kirigami Structures for Multimodal Integration

A deformable, kirigami electrical interconnect is employed to integrate the mechanical and thermal haptic subsystems while enabling large stretchability. Building on our previous optimization of kirigami structures [28], a serial pattern kirigami structure is adopted with a thickness of 1.5 mm, cut length of 5 mm, cut spacing of 2 mm, hinge length of 2.75 mm, and cut width of 70 µm (Figure 4h). A 0.3-mm-wide gallium channel is embedded along the kirigami pattern, serving as the mechanically compliant electrical bridge to connect the thermo-haptic unit with surrounding mechano-haptic units. The liquid nature of the gallium at skin temperature provides over 120% stretchability with stable electrical resistance (Figure S8). Under tensile strain, the kirigami structure accommodates most strain, relieving the strain experienced by the mechano- and thermo-haptic units [62]. To evaluate the mechanical and thermal robustness of the kirigami-enabled system under deformation, the device performance was characterized at applied tensile strain (Figure 4i–l). The actuation displacement exhibits a slight decrease with increasing strain (Figure 4i), with a similar trend observed for the output force (Figure 4j). These results indicate that mechanical actuation performance is only weakly affected by structural elongation. In addition, the thermal output remains highly stable under strain. The heating temperature (Figure 4k) shows negligible variation (~ 42°C–43°C), while the cooling temperature (Figure 4l) shows only a minimal increase across the entire strain range. The small variation suggests that the thermal functionality is largely insensitive to system-level mechanical deformation. Overall, the kirigami architecture effectively decouples mechanical deformation from functional performance, enabling almost strain-invariant haptic output. This structural design ensures reliable operation under stretching conditions, a critical requirement for skin-integrated applications.

2.6 | Multimodal Haptic Interfaces for Reconstruction of Tactile Sensation in Virtual Reality

The integrated multimodal haptic interface enables tactile reconstruction by concurrently activating thermal and mechanical sensations. In a kitchen-like VR scenario, the user interacted with virtual objects through a VR headset while coordinated haptic feedback was delivered by the wearable interface mounted on the forearm (Figure 5a,b). The virtual scene included five representative object materials to provide distinct Young's modulus E and thermal conductivities k (Figure 5c and Table S4). To reproduce these differences, the amplitudes of the mechano-haptic unit were programmed according to the Young's modulus of the object materials (Figure 5d), while the thermo-haptic unit rendered material-dependent thermal cues based on their thermal conductivities (Figure 5e), generating distinct temperature profiles during contact (Figure 5f).

2.6.1 | Mechano-Haptic Rendering

Each material's Young's modulus E was mapped to haptic actuator displacements on a perceptually appropriate scale by first compressing E with a base-10 logarithm, and then normalizing over the modulus span of the materials with a dimensionless normalized stiffness index t:

$$t = \frac{\log_{10}(E) - \log_{10}(E_{\min})}{\log_{10}(E_{\max}) - \log_{10}(E_{\min})},\ t \in [0, 1] \tag{2}$$

where $E_{\min} = 0.002$ GPa and $E_{\max} = 72$ GPa. Since stiffer materials generate smaller skin deformation during physical interaction, this index is inverted and mapped it to the actuator's available displacement range $A_{\min}, A_{\max}$ using a shaping exponent γ.

$$A(E) = A_{\min} + (1 - t)^{\gamma}[A_{\max} - A_{\min}] \tag{3}$$

where $A_{\min} = 0.6$ mm, $A_{\max} = 2.7$ mm, and γ is set to 0.6 to enhance the separability among high E materials without saturating the haptic response at the softer end of the spectrum (Figure S9).

2.6.2 | Thermo-Haptic Rendering

The thermal profiles of the transient cooling of the skin surface after contacting different materials initially at room temperature can be analyzed using a semi-infinite, 1-D conduction model with a finite interfacial heat transfer coefficient h. In this model, the skin is treated as a semi-infinite medium, and the interface heat exchange is described by a convective boundary condition [12]. Under these assumptions, the transient skin-facing temperature can be expressed as

$$T_{\text{skin}} = T_{\text{s,i}} - \frac{T_{\text{s,i}} - T_{\text{o,i}}}{1 + \frac{e_{\text{skin}}}{e_{\text{obj}}}} \left[1 - \exp\left(\left(\frac{h}{k_{\text{skin}}}\right)^2 \text{erfc}\left(\frac{h}{k_{\text{skin}}}\right)\sqrt{\alpha_{\text{skin}} t}\right)\right] \tag{4}$$

where $T_{\text{s,i}}$ and $T_{\text{o,i}}$ are the initial temperature of skin and object, respectively. e_{skin} and e_{obj} represent the thermal effusivity of skin and object, respectively, which characterizes the ability of a material to exchange heat with its surroundings. k_{skin} is the thermal conductivity of the skin. α_{skin} is the skin thermal diffusivity, which is the rate of heat propagation. t is the time after initial contact. The exponential erfc factor accounts for the decay of the temperature difference due to diffusion within the skin and the finite interfacial conductance. This model implies that object materials with high thermal effusivity and strong interfacial conductance (e.g., aluminum) draw heat rapidly from the skin, producing a colder sensation. Conversely, low-effusivity materials (e.g., PDMS, printing paper) exchange heat more slowly, yielding a weaker thermal perception.

2.6.3 | Multimodal Haptic Perception for Material Recognition

Participants were asked to wear a VR headset and the skin-integrated multimodal haptic device on the forearm (Figure 5a,b). When the participant contacted each object in the VR environment (Figure 5c), corresponding haptic stimuli were delivered on the skin via the haptic interface. Specifically, the displacement amplitudes generated by the mechano-haptic unit for each object are summarized in Figure 5d. The highest amplitude was encoded for PDMS, with the lowest for glass. The average deviation between designed and experimental amplitudes is approximately 2.5%, indicating accurate amplitude control and reliable mechanical rendering. A detailed relationship between the mapped vibration amplitude and Young's modulus is provided in Figure 5d and Figure S9. The skin-contact temperature profiles predicted by Equation (4) (Figure 5e) for each material are presented in Figure S10. Aluminum is predicted to produce the largest temperature drop, reaching approximately 21.1°C at 30 s, whereas printing paper exhibits the smallest decrease with a final temperature of approximately 29.5°C. These results highlight that

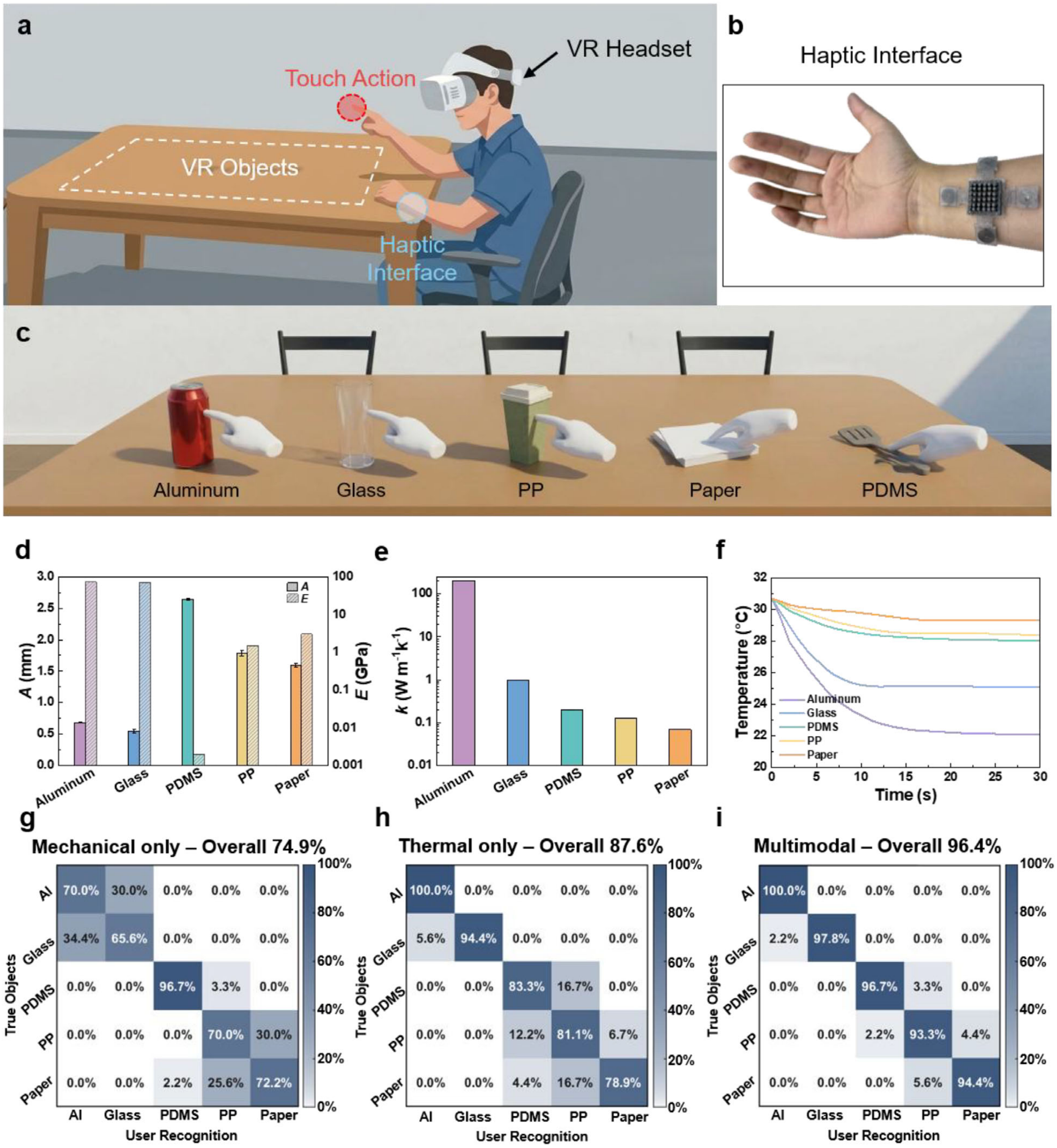

FIGURE 5 | Reconstruction of artificial tactile sensation with skin-integrated multimodal haptic device in VR space. (a) Experimental setup of the VR-based multimodal haptic perception system. (b) Detailed view of the device positioned on the user's forearm. (c) First-person VR view of different objects. (d) Displacement amplitude (***A***) of the mechano-haptic unit mapped from the Young's modulus (***E***) of each material, with error bars indicating experimental variability. (e) Summary of thermal conductivities (***k***) of different materials. (f) Experimentally generated thermal profiles by the thermo-haptic unit corresponding to the heat transfer characteristics during skin contact for each material. Confusion matrices of material recognition performance under three conditions: (g) mechano-haptic stimulation was provided, (h) thermo-haptic stimulation was provided, and (i) both mechano- and thermo- haptic stimulation was provided. Overall accuracy was calculated as the proportion of correctly identified trials among all trials.

different materials produce distinct skin contact temperature profiles, reflecting an important thermal characteristic of material perception that cannot be captured by mechanical cues. The corresponding experimental temperature profiles generated by the thermo-haptic unit are shown in Figure 5f. All curves exhibit an initial rapid temperature decrease upon contact, followed by a gradual approach to a steady plateau. The trends in the initial cooling behavior and final steady temperature are consistent with the simulation predictions, indicating that the haptic device was able to accurately reproduce the material-specific thermal response characteristics.

In the user study, after an initial training and practice session (see Experimental Section for details), three adult participants were asked to identify five virtual object materials based on mechanical and thermal cues from the haptic interface, with visual cues blocked during testing. The study was conducted under three stimulus conditions: mechanical cues only, thermal cues only, and combined mechanical and thermal cues. For each participant, the experiment included 150 trials per condition and 450 trials across the three stimulus conditions. Across the three participants, this resulted in 450 trials per condition and 1350 trials in total. The resulting confusion matrices are shown in Figure 5g–i. When only mechanical cues were provided, the overall classification accuracy was 74.9% (Figure 5g). Significant confusion was observed between aluminum and glass, which were frequently misclassified as each other because both exhibit similarly high stiffness (small vibration amplitude). Furthermore, mutual misclassification occurred: 30.0% of PP samples were misidentified as paper, and 25.6% of paper samples were misidentified as PP; 2.2% of paper samples were misidentified as PDMS. These results suggest that the mechano-haptic stimuli alone are insufficient for reliable discrimination between materials with comparable stiffness or compliance.

Thermal-cues-only haptic feedback substantially improved classification accuracy, increasing the overall performance to 87.6% (Figure 5h). This approach was highly effective for discriminating materials with high thermal conductivity and apparently different thermal profiles, with classification accuracies of 100.0% for aluminum and 94.4% for glass, demonstrating that thermal transient signals provide a robust basis for separating these materials. However, misclassification between polymeric materials still exists, with 16.7% of PDMS being misidentified as PP, and 12.2% of PP being misclassified as PDMS.

To address these remaining ambiguities, the integration of both mechanical and thermal stimuli is necessary. The multimodal approach resulted in a strongly diagonal confusion matrix and an overall accuracy of 96.4%, as shown in Figure 5i. For instance, aluminum and glass, with their similar Young's modulus, are easily confused in mechano-haptic-only mode; however, their greatly different thermal conductivities allow them to be perfectly distinguished when thermo-haptic cues are introduced. The confusion between materials was substantially resolved, with PP and paper being correctly identified with recognition rates of 93.3% and 94.4%, respectively. Ultimately, the combination of haptic modalities effectively eliminated the key ambiguities present in single-cue conditions. Ultimately, the combination of haptic modalities effectively eliminated the key ambiguities present in single-cue conditions. Multimodal haptic interfaces significantly improve material recognition by simultaneously triggering the skin's mechanoreceptors and thermoreceptors. To place these results in context, Table S1 summarizes representative haptic perception studies related to material or object recognition. Many prior systems have incorporated wearable, skin-contact, or glove-integrated formats toward skin-conformal haptic interfaces. However, the reported perception tasks and evaluation metrics vary across studies, and few systems quantitatively compare blinded multi-material recognition under mechanical-only, thermal-only, and combined multimodal conditions. In contrast, the skin-integrated device in this work was evaluated under all three stimulus conditions, directly demonstrating the benefit of multimodal feedback for material recognition.

After evaluating the thermal, mechanical, and user-perception performance of the integrated device, we further compared our device with representative wearable thermal and multimodal haptic platforms (Table S2). Reported bidirectional heating/cooling devices show response times ranging from single-digit seconds to several minutes; our platform operates within the faster region of this range, with 18 s heating and 20 s cooling over a skin-compatible temperature window of 10°C–40°C. Among the devices compared, only a small subset reports co-located electromechanical actuation, yet their mechanical output is too limited to sufficiently trigger haptic feedback on the skin [16, 19, 63]. Among multimodal haptic systems, only two heating-only systems demonstrate substantial stretchability, but both lack active cooling capabilities [16, 19]. Specifically, the skin-integrated wireless thermo-haptic system reported by Kim et al. combines a thermoelectric cell with an ERM vibrotactile actuator. The paper reports vibrotactile displacement, but does not provide the actuation force or cycling stability [63]. By comparison, our device combines bidirectional thermal actuation, a compliant Ga/PDMS heat sink, quantified co-located mechanical output, and a strain tolerance matching the sink's elastic range in both subsystems.

3 | Conclusion

In this work, we present a skin-integrated soft heating and cooling device comprising a BN/paraffin/polymer thermal interface and a flexible Ga/PDMS pin-fin heat sink for efficient thermal management. When integrated with a liquid-metal electromagnetic actuator via a Ga-filled kirigami interconnect, the resulting multimodal haptic device enables programmable thermal and mechanical feedback within a conformal platform. The integrated system achieves robust thermal and mechanical performance, including rapid and reversible thermal responses, large out-of-plane displacement and force, and durable actuation over more than 1,000 cycles and under tensile strain. User studies demonstrated that multimodal feedback significantly enhances material perception: Recognition accuracy improved from 74.9% (mechanical-only) and 87.6% (thermal-only) to 96.4% with simultaneous feedback, proving that coupled cues effectively reduce perceptual ambiguity. This study establishes versatile materials and integration strategies for skin-integrated multimodal haptic interfaces. Such platforms could support highly realistic tactile interactions in virtual and augmented reality, telepresence, and future wearable systems designed to augment or restore haptic perception.

Beyond VR/AR, skin-conformal thermo-mechanical haptic interfaces could support telepresence, medical rehabilitation, bionic prosthetics, surgical robotics, teleoperation, and human-robot interaction, where coordinated thermal and mechanical feedback can provide more task-relevant tactile information. Next-generation systems require improved sensor-actuator integration, higher spatial and temporal resolution, advanced wireless and low-power operation, closed-loop temperature and force control, and adaptive feedback that accounts for the user, task, and skin-contact condition. Practical deployment will also require careful thermal safety control, lower power consumption, long-term mechanical durability, stable epidermal contact under deformation, device-to-device uniformity, and scalable fabrication.

4 | Experimental Section

4.1 | Materials

PDMS (Dow Sylgard 184) was obtained from Ellsworth Adhesives. Hexagonal boron nitride (h-BN, 35–45 µm) was purchased from Matexcel. Phase change materials (paraffin) with different melting points were purchased from Blended Waxes, Inc. and Hainan Coinno Intelligent Technology Co., Ltd. Silver ink (127-07) was purchased from Creative Materials. Span 80 was obtained from Sigma–Aldrich. $Sn_{42}/Bi_{57.6}/Ag_{0.4}$ solder paste was purchased from Chip Quik Inc. Liquid metal (Gallium, Ga) was purchased from Gallent Metals. Wax was purchased from SAEUYVB. Ecoflex (0030) and Smooth-On Sil-Poxy glue were obtained from Smooth-On. Bi_2Te_3 thermoelectric pellets were obtained from Wuhan XinRong New Materials. All materials were used as received.

4.2 | Fabrication of Skin Thermal Interface

The h-BN/paraffin/PDMS composite used as the skin thermal interface was prepared as follows. First, 2 g of PDMS base was mixed with hexagonal boron nitride (h-BN) at loadings of 10, 20, 30, and 35 wt.% (relative to the PDMS base), together with Span 80 (5 wt.% of the PDMS/BN mixture) to improve paraffin dispersion. The mixture was processed in a planetary mixer (Thinky, AR-100) at 2000 rpm for 2 min. Next, paraffin was introduced at 20, 25, and 30 wt.% relative to the PDMS base and mixed again at 2000 rpm for 2 min. The PDMS curing agent was then added at a weight ratio of 1:10 (curing agent: base), followed by the same mixing step and vacuum degassing to ensure uniform paraffin distribution. The resulting slurry was cast onto a glass substrate serving as a release surface, with the wet film thickness set to 0.2 mm. The coated film was allowed to rest at room temperature for 2 min to release trapped bubbles and then cured on a hot plate at 80°C for 30 min to obtain a flat, fully cross-linked film.

4.3 | Fabrication of Soft Heat Sink

First, a 3D-printed master (Prusa Research, i3 MK3S+) was prepared and used to cast an Ecoflex negative replica. Next, a wax positive was cast from the Ecoflex negative to serve as a sacrificial mold. A Ga/PDMS composite was then formulated by mixing PDMS with gallium at a 1:3 weight ratio, followed by stirring and degassing. The curing agent was then added at 1:40 (w/w, relative to the mixture). This final composite was poured into the wax mold and degassed again to minimize voids. After standing for 24 h, the assembly was heated to 80°C to melt the wax and release the pin-fin heat-sink structure (Figure S2).

4.4 | Integration of TEM

For TEM integration, the PDMS composite substrate incorporating BN and paraffin was first cured on a hot plate at 80°C for 30 min. To enhance adhesion between the printed conductive layer and the PDMS substrate, the surface was treated with oxygen plasma (100 W, 0.3 mbar, 60 s) and then immersed in a 2% (v/v) GPTMS solution in isopropanol/deionized water (95:5, v/v) for around 2 min. The substrate was subsequently dried with nitrogen and baked at 80°C for 10 min. A rectangular interconnect pattern (4.6×1.5 mm^2) was then defined using a shadow mask, and stretchable silver ink was stencil printed onto the treated substrate. This length was chosen to electrically bridge two adjacent thermoelectric pellets, each with a lateral size of 1.4×1.4 mm^2 and a gap of 1.6 mm between them. Thermoelectric pellets with dimensions of 1.4 mm × 1.4 mm × 1.7 mm were assembled into a 6 × 6 interconnection array. A second shadow mask was then used to define the solder deposition areas. Low-temperature $Sn_{42}/Bi_{57.6}/Ag_{0.4}$ solder paste was applied in a 1.5×1.5 mm^2 pattern to bond each thermoelectric pellet to the underlying silver interconnects. The pellets were placed onto the solder-coated regions and thermally reflowed to fix one side, after which the opposite side was connected using the same procedure. The curing and reflow processes were carried out using a stepped thermal profile of 80°C, 120°C, and 175°C, with a holding time of 2 min at each temperature.

4.5 | Fabrication of Soft Electromagnetic Haptic Actuator

The essential component of the haptic actuator is a Ga coil encapsulated in Ecoflex, which generates the magnetic field upon current application. To start the fabrication, Ecoflex precursor (parts A:B = 1:1 by weight) was poured onto a 3D-printed (Prusa Research, i3 MK3S+) mold defining the coil microchannel and thermally cured at 80°C for 1 h. A sealing film was prepared by spin-coating (Laurell, WS-650Mz-23NPPB) with the same Ecoflex precursor onto a substrate at 500 rpm for 1 min, followed by curing at 80°C for 1 h. The cured channel layer and the sealing thin film were laminated using a small amount of uncured Ecoflex applied at the interface as an adhesive. The channels were then filled with molten Ga, and copper leads were embedded at the coil center and the terminal end to provide electrical connection. A permanent magnet was placed above the Ga coil and confined between the coil layer and an Ecoflex soft membrane. The soft membrane (with a thickness of 150 µm) contained a shallow groove to accommodate the magnet and maintain its position during actuation. The four corners of the membrane were bonded to the actuator structure, which prevented magnet flipping and ensured stable mechanical coupling between the magnet and the coil.

4.6 | Integration of Multimodal Haptic Interface by Kirigami Springs

Kirigami spring elements were fabricated from Ecoflex (parts A:B = 1:1 by weight). Before fabrication, a UV-cured printed mold (Shenzhen Anycubic Technology Co., Ltd, Anycubic Photon M3 Plus) was printed to define both the kirigami geometry and the embedded microchannels for Ga interconnects. The mixed Ecoflex precursor was cast into the mold and then cured at 80°C for 1 h. An Ecoflex sealing film was produced by spin-coating the liquid precursor at 500 rpm for 1 min and cured under the same conditions. The kirigami interconnects with microchannels and sealing film were bonded using a thin layer of uncured Ecoflex as adhesive. After bonding, the microchannels were filled with molten Ga to complete the fabrication of the interconnection. Then, the Smooth-On Sil-Poxy glue was used as the bonding adhesive to integrate the mechanical, thermal, and kirigami components. The overall device footprint is 62 × 62 mm^2.

4.7 | VR Environment Setup

The VR testing environment was created with C# in Unity. Unity's XR Interaction Toolkit Demo Scene was modified to create a kitchen-like virtual environment with assets from the Unity Asset Store. Communication between Unity and the Arduino was implemented using the Ardity package, enabling user interactions with the virtual kitchen objects. Informed signed consent for this demonstration was obtained from the volunteer before participation in this study.

4.8 | Multimodal Stimuli Experiment Design

Three adult volunteers participated in this preliminary proof-of-concept user study. Informed consent was obtained from all participants before the study. During formal testing, participants were blinded to the target material identity for each trial, visual cues were blocked, and no correctness feedback was provided. Because the experimenter was aware of the stimulus condition and target material, the study was participant-blinded rather than double-blinded. We evaluated material identification using a multimodal haptic interface that delivered mechanical and thermal cues to participants' forearms. Mechanical stimulation was generated by the mechano-haptic units using electromagnetic actuators, with the indentation amplitude controlled by the driving current. Thermal stimulation was produced by the thermo-haptic unit based on TEM, with temperature regulated by current control and monitored by a thermocouple placed on the surface of the thermo-haptic unit. Three stimulus conditions were tested: mechano-haptic-only, thermo-haptic-only, and combined mechano- and thermo-haptic stimulation. Before each trial, the mechano-haptic actuator was returned to its initial position, and the thermo-haptic unit was reset to a baseline temperature of 33°C. Each stimulus lasted 3 s, consisting of approximately 1 s press, 1 s hold, and 1 s release for mechano-haptic units. The temperature output of the thermo-haptic unit was limited to 20°C–45°C. Consecutive trials were separated by 15–25 s to allow the thermo-haptic unit to return to baseline, and short breaks were provided every 10–15 trials to prevent user fatigue.

Before formal testing, participants completed a training phase followed by a practice phase. In the training phase, labeled demonstrations were provided for each stimulus condition and each material to familiarize participants with the correspondence between the haptic cues and the materials. In the practice phase, three blocks were conducted for each condition. In each block, the five materials were each presented once in randomized order, with the constraint that the same material did not appear in consecutive trials. After each presentation, participants identified the material and rated their confidence on a five-point scale. Correctness feedback was provided during practice. Participants proceeded to the formal testing once the following criteria were met: classification accuracy ≥ 60%, median confidence on correct trials ≥ 3, median confidence on incorrect trials ≤ 3, and high confidence error ratio ≤ 10%. High confidence error ratio is calculated by normalizing total high confidence errors (incorrect trials with confidence ≥ 4) to the total number of practice trials.

In the formal testing phase, the same three stimulus conditions were evaluated without correctness feedback. For each participant and each condition, six blocks were conducted. In each block, each of the five materials was presented five times, yielding 25 trials per block and 150 trials per condition per participant. For each participant, the three stimulus conditions resulted in 450 trials in total. Across the three participants, this resulted in 450 trials per condition and 1350 trials in total. The trial order within each block was randomized with the constraint that the same material did not appear in consecutive trials. After each trial, participants reported the perceived material and their confidence rating. Performance was summarized using confusion matrices, where rows correspond to the true material and columns correspond to the participant-identified material. Overall accuracy was calculated as the proportion of correctly identified trials among all trials. Row-normalized heat maps were used for visualization. The material-recognition experiment relied on participants' categorical responses rather than on a machine-learning classification model. For each trial, the true material, stimulus condition, participant response, confidence rating, and trial order were recorded. Performance was analyzed at the behavioral-response level using the confusion matrices and overall accuracy described above. The error rate was defined as one minus the overall accuracy.

4.9 | Characterization

All temperature-time profiles were recorded with a type-K thermocouple (Omega Engineering, HH802U) in contact with the device surface. IR images were acquired using a thermal camera (FLIR, FLIR A325sc) with an emissivity setting of 0.95. The thermal conductivity of the BN/PDMS and BN/paraffin/PDMS composites was measured using a steady-state through-plane heat-flow method. The composite sample was placed in series with a calibrated heat-flux sensor between two temperature-controlled TEC plates. After the system reached steady state under a small temperature difference, the heat flux and the temperature difference between the hot and cold sides were recorded. The composite thermal conductivity was calculated using a one-dimensional thermal-resistance model, as described in Figure S11 [64]. Displacement was measured by a laser displacement sensor (KEYENCE, IL-S025). Thermal and mechanical actuation tests were driven by a DC power supply (Agilent Technologies, Triple-output DC power supply). To characterize the actuation performance of the haptic actuator at different frequencies, a custom switchboard controller was employed in conjunction with the DC power source to generate sinusoidal currents ranging from 1 to 50 Hz. All measurements were repeated at least 5 times. Data are presented as mean ± standard deviation, and the error bars represent the standard deviation.

Acknowledgements

This material was based upon work supported by the National Science Foundation under Award No. ECCS-2238363. S.Y. would like to acknowledge the support from the start-up fund at Stony Brook University. The authors gratefully acknowledge Professor Lifeng Wang and his student Shaodi Wu for their assistance with 3D printing, as well as Professor David Hwang and his student Yiting Zheng for their assistance with thermal conductivity measurements. All contributors are from the Department of Mechanical Engineering at Stony Brook University.

Conflicts of Interest

The authors declare no conflicts of interest.

Data Availability Statement

The data that support the findings of this study are available from the corresponding author upon reasonable request.

References

1. L. E. Osborn, R. Venkatasubramanian, M. Himmtann, et al., "Evoking Natural Thermal Perceptions Using a Thin-Film Thermoelectric Device With High Cooling Power Density and Speed," *Nature Biomedical Engineering* 8, no. 8 (2024): 1004–1017, https://doi.org/10.1038/s41551-023-01070-w.

2. V. E. Abraira and D. D. Ginty, "The Sensory Neurons of Touch," *Neuron* 79, no. 4 (2013): 618–639, https://doi.org/10.1016/j.neuron.2013.07.051.

3. R. J. Schepers and M. Ringkamp, "Thermoreceptors and Thermosensitive Afferents," *Neuroscience & Biobehavioral Reviews* 34, no. 2 (2010): 177–184, https://doi.org/10.1016/j.neubiorev.2009.10.003.

4. K.-H. Ha, J. Yoo, S. Li, et al., "Full Freedom-of-Motion Actuators as Advanced Haptic Interfaces," *Science* 387, no. 6741 (2025): 1383–1390, https://doi.org/10.1126/science.adt2481.

5. Q. Liu, S. Ghodrat, G. Huisman, and K. M. B. Jansen, "Shape Memory Alloy Actuators For Haptic Wearables: A Review," *Materials & Design* 233 (2023): 112264, https://doi.org/10.1016/j.matdes.2023.112264.

6. M. Zhu, S. Biswas, S. I. Dinulescu, N. Kastor, E. W. Hawkes, and Y. Visell, "Soft, Wearable Robotics and Haptics: Technologies, Trends, and Emerging Applications," *Proceedings of the IEEE* 110, no. 2 (2022): 246–272, https://doi.org/10.1109/jproc.2021.3140049.

7. S. Patel, Z. Rao, M. Yang, and C. Yu, "Wearable Haptic Feedback Interfaces for Augmenting Human Touch," *Advanced Functional Materials* 36, no. 6 (2025): 2417906, https://doi.org/10.1002/adfm.202417906.

8. Y. Huang, K. Yao, J. Li, et al., "Recent Advances in Multi-Mode Haptic Feedback Technologies Towards Wearable Interfaces," *Materials Today Physics* 22 (2022): 100602, https://doi.org/10.1016/j.mtphys.2021.100602.

9. K. Kim, "A Review of Haptic Feedback Through Peripheral Nerve Stimulation for Upper Extremity Prosthetics," *Current Opinion in Biomedical Engineering* 21 (2022): 100368, https://doi.org/10.1016/j.cobme.2022.100368.

10. T. H. Yang, J. R. Kim, H. Jin, H. Gil, J. H. Koo, and H. J. Kim, "Recent Advances and Opportunities of Active Materials for Haptic Technologies in Virtual and Augmented Reality," *Advanced Functional Materials* 31, no. 39 (2021): 2008831, https://doi.org/10.1002/adfm.202008831.

11. Y. Huang, J. Zhou, P. Ke, et al., "A Skin-Integrated Multimodal Haptic Interface For Immersive Tactile Feedback," *Nature Electronics* 6, no. 12 (2023): 1020–1031, https://doi.org/10.1038/s41928-023-01074-z.

12. J. Lee, H. Sul, W. Lee, et al., "Stretchable Skin-Like Cooling/Heating Device for Reconstruction of Artificial Thermal Sensation in Virtual Reality," *Advanced Functional Materials* 30, no. 29 (2020): 1909171, https://doi.org/10.1002/adfm.201909171.

13. M. Bohic and V. E. Abraira, "Wired for Social Touch: The Sense That Binds us to Others," *Current Opinion in Behavioral Sciences* 43 (2022): 207–215, https://doi.org/10.1016/j.cobeha.2021.10.009.

14. S. Chen, Y. Chen, J. Yang, T. Han, and S. Yao, "Skin-Integrated Stretchable Actuators Toward Skin-Compatible Haptic Feedback and Closed-Loop Human-Machine Interactions," *npj Flexible Electronics* 7, no. 1 (2023): 1, https://doi.org/10.1038/s41528-022-00235-y.

15. M. Park, J.-Y. Yoo, T. Yang, et al., "Skin-Integrated Systems For Power Efficient, Programmable Thermal Sensations Across Large Body Areas," *Proceedings of the National Academy of Sciences* 120, no. 6 (2023): 2217828120, https://doi.org/10.1073/pnas.2217828120.

16. J. Oh, S. Kim, S. Lee, S. Jeong, S. H. Ko, and J. Bae, "A Liquid Metal Based Multimodal Sensor and Haptic Feedback Device for Thermal and Tactile Sensation Generation in Virtual Reality," *Advanced Functional Materials* 31, no. 39 (2021): 2007772, https://doi.org/10.1002/adfm.202007772.

17. B. W. An, E.-J. Gwak, K. Kim, et al., "Stretchable, Transparent Electrodes as Wearable Heaters Using Nanotrough Networks of Metallic Glasses With Superior Mechanical Properties and Thermal Stability," *Nano Letters* 16, no. 1 (2016): 471–478, https://doi.org/10.1021/acs.nanolett.5b04134.

18. Y. Wang, Z. Yu, G. Mao, et al., "Printable Liquid-Metal@PDMS Stretchable Heater With High Stretchability and Dynamic Stability for Wearable Thermotherapy," *Advanced Materials Technologies* 4, no. 2 (2019): 1800435, https://doi.org/10.1002/admt.201800435.

19. J. Zhou, M. Mulle, Y. Zhang, et al., "High-Ampacity Conductive Polymer Microfibers as Fast Response Wearable Heaters and Electromechanical Actuators," *Journal of Materials Chemistry C* 4, no. 6 (2016): 1238–1249, https://doi.org/10.1039/C5TC03380B.

20. D. Kim, J. Bang, W. Lee, et al., "Highly Stretchable and Oxidation-Resistive Cu Nanowire Heater for Replication of the Feeling of Heat in a Virtual World," *Journal of Materials Chemistry A* 8, no. 17 (2020): 8281–8291, https://doi.org/10.1039/D0TA00380H.

21. Y. Han, L. E. Simonsen, and M. H. Malakooti, "Printing Liquid Metal Elastomer Composites for High-Performance Stretchable Thermoelectric Generators," *Advanced Energy Materials* 12, no. 34 (2022): 2201413, https://doi.org/10.1002/aenm.202201413.

22. S. Hong, H. Lee, J. Lee, et al., "Highly Stretchable and Transparent Metal Nanowire Heater for Wearable Electronics Applications," *Advanced Materials* 27, no. 32 (2015): 4744–4751, https://doi.org/10.1002/adma.201500917.

23. B. Sun and X. Huang, "Seeking Advanced Thermal Management for Stretchable Electronics," *npj Flexible Electronics* 5, no. 1 (2021): 12, https://doi.org/10.1038/s41528-021-00109-9.

24. Z. Shen and J. Feng, "Achieving Vertically Aligned SiC Microwires Networks in a Uniform Cold Environment for Polymer Composites With High Through-Plane Thermal Conductivity Enhancement," *Composites Science and Technology* 170 (2019): 135–140, https://doi.org/10.1016/j.compscitech.2018.11.036.

25. J. Liu, W. Li, Y. Guo, H. Zhang, and Z. Zhang, "Improved Thermal Conductivity of Thermoplastic Polyurethane via Aligned Boron Nitride Platelets Assisted by 3D Printing," *Composites Part A: Applied Science and Manufacturing* 120 (2019): 140–146, https://doi.org/10.1016/j.compositesa.2019.02.026.

26. S. Hong, Y. Gu, J. K. Seo, et al., "Wearable Thermoelectrics for Personalized Thermoregulation," *Science Advances* 5, no. 5 (2019): aaw0536, https://doi.org/10.1126/sciadv.aaw0536.

27. J. Cui and S. Zhou, "Facile Fabrication of Highly Conductive Polystyrene/Nanocarbon Composites With Robust Interconnected Network via Electrostatic Attraction Strategy," *Journal of Materials Chemistry C* 6, no. 3 (2018): 550–557, https://doi.org/10.1039/C7TC04752E.

28. D. Zou, X. Huang, Y. Zhu, J. Chen, and P. Jiang, "Boron Nitride Nanosheets Endow the Traditional Dielectric Polymer Composites With Advanced Thermal Management Capability," *Composites Science and Technology* 177 (2019): 88–95, https://doi.org/10.1016/j.compscitech.2019.04.027.

29. D. Pan, S. Luo, Y. Feng, et al., "Highly Thermally Conductive 3D BN/MWCNTs/C Spatial Network Composites With Improved Electrically Insulating and Flame Retardancy Prepared by Biological Template

Assisted Method," *Composites Part B: Engineering* 222 (2021): 109039, https://doi.org/10.1016/j.compositesb.2021.109039.

30. X. Zhuang, Y. Zhou, and F. Liu, "A Novel 3D Sandwich Structure of Hybrid Graphite Nanosheets and Silver Nanowires as Fillers for Improved Thermal Conductivity," *Materials Research Express* 4, no. 1 (2017): 015018, https://doi.org/10.1088/2053-1591/aa55b3.

31. E.-C. Cho, C.-W. Chang-Jian, Y.-S. Hsiao, K.-C. Lee, and J.-H. Huang, "Three-Dimensional Carbon Nanotube Based Polymer Composites for Thermal Management," *Composites Part A: Applied Science and Manufacturing* 90 (2016): 678–686, https://doi.org/10.1016/j.compositesa.2016.08.035.

32. Z. Wang, Z. Wu, L. Weng, et al., "A Roadmap Review of Thermally Conductive Polymer Composites: Critical Factors, Progress, and Prospects," *Advanced Functional Materials* 33, no. 36 (2023): 2301549, https://doi.org/10.1002/adfm.202301549.

33. C. Li, L. Qiu, B. Zhang, D. Li, and C. Y. Liu, "Robust Vacuum-/Air-Dried Graphene Aerogels and Fast Recoverable Shape-Memory Hybrid Foams," *Advanced Materials* 28, no. 7 (2016): 1510–1516, https://doi.org/10.1002/adma.201504317.

34. X. Leng, C. Xiao, L. Chen, et al., "An Efficient Approach for Constructing 3-D Boron Nitride Networks With Epoxy Composites to Form Materials With Enhanced Thermal, Dielectric, and Mechanical Properties," *High Performance Polymers* 31, no. 3 (2019): 350–358, https://doi.org/10.1177/0954008318772331.

35. J. Chen, H. Wei, H. Bao, P. Jiang, and X. Huang, "Millefeuille-Inspired Thermally Conductive Polymer Nanocomposites With Overlapping BN Nanosheets for Thermal Management Applications," *ACS Applied Materials & Interfaces* 11, no. 34 (2019): 31402–31410, https://doi.org/10.1021/acsami.9b10810.

36. Q. Sun, G. Zhi, S. Zhou, et al., "Advanced Design and Manufacturing Approaches for Structures With Enhanced Thermal Management Performance: A Review," *Advanced Materials Technologies* 9, no. 15 (2024): 2400263, https://doi.org/10.1002/admt.202400263.

37. Z. Xu, C. Li, H. Zhao, Y. Zheng, and J. Zhang, "Design and Performance Analysis of Hot Side Heat Sink of Thermoelectric Cooler Device Based on Simulation and Experiment," *Energy Science & Engineering* 11, no. 12 (2023): 4463–4480, https://doi.org/10.1002/ese3.1591.

38. R. A. Kishore, A. Nozariasbmarz, B. Poudel, M. Sanghadasa, and S. Priya, "Ultra-High Performance Wearable Thermoelectric Coolers With Less Materials," *Nature Communications* 10, no. 1 (2019): 1765, https://doi.org/10.1038/s41467-019-09707-8.

39. J. Mao, H. Zhu, Z. Ding, et al., "High Thermoelectric Cooling Performance of n-type Mg_3Bi_2-Based Materials," *Science* 365, no. 6452 (2019): 495–498, https://doi.org/10.1126/science.aax7792.

40. K. Kim, S. Choo, J. Lee, et al., "Heat-Dissipation Design and 3D Printing of Ternary Silver Chalcogenide-Based Thermoelectric Legs for Enhancing Power Generation Performance," *Advanced Science* 11, no. 30 (2024): 2402934, https://doi.org/10.1002/advs.202402934.

41. Y. Qiu, Z. Lu, and Q. Pei, "Refreshable Tactile Display Based on a Bistable Electroactive Polymer and a Stretchable Serpentine Joule Heating Electrode," *ACS Applied Materials & Interfaces* 10, no. 29 (2018): 24807–24815, https://doi.org/10.1021/acsami.8b07020.

42. I. Choi, E. Ofek, H. Benko, M. Sinclair, and C. Holz, "Claw: A Multifunctional Handheld Haptic Controller for Grasping, Touching, and Triggering in Virtual Reality," in *Proceedings of the 2018 CHI conference on human factors in computing systems* (Association for Computing Machinery, 2018), 1–13, https://doi.org/10.1145/3173574.3174228.

43. M. Gabardi, D. Chiaradia, D. Leonardis, M. Solazzi, and A. Frisoli, "A High Performance Thermal Control for Simulation of Different Materials in a Fingertip Haptic Device," in *International Conference on Human Haptic Sensing and Touch Enabled Computer Applications* (Springer, 2018), 313–325, https://doi.org/10.1007/978-3-319-93399-3_28.

44. A. Mazzotta, M. Carlotti, and V. Mattoli, "Conformable On-Skin Devices for Thermo-Electro-Tactile Stimulation: Materials, Design, and Fabrication," *Materials Advances* 2, no. 6 (2021): 1787–1820, https://doi.org/10.1039/D0MA00817F.

45. Tellurex Corporation, *The Most Frequently Asked Questions About Thermoelectric Cooling* (Tellurex Corporation, 2006).

46. T. L. Bergman, *Fundamentals of Heat and Mass Transfer* (John Wiley & Sons, 2011).

47. D. M. Rowe, *Thermoelectrics Handbook: Macro to Nano* (CRC Press, 2006).

48. E. K. Sichel, R. E. Miller, M. S. Abrahams, and C. J. Buiocchi, "Heat Capacity and Thermal Conductivity of Hexagonal Pyrolytic Boron Nitride," *Physical Review B* 13, no. 10 (1976): 4607–4611, https://doi.org/10.1103/PhysRevB.13.4607.

49. Z. Qian, H. Shen, X. Fang, L. Fan, N. Zhao, and J. Xu, "Phase Change Materials of Paraffin in h-BN Porous Scaffolds With Enhanced Thermal Conductivity and Form Stability," *Energy and Buildings* 158 (2018): 1184–1188, https://doi.org/10.1016/j.enbuild.2017.11.033.

50. X. Liu and Z. Rao, "Interfacial Thermal Conductance Across Hexagonal Boron Nitride & Paraffin Based Thermal Energy Storage Materials," *Journal of Energy Storage* 32 (2020): 101860, https://doi.org/10.1016/j.est.2020.101860.

51. B. Feng, Y.-H. Zhang, J. Tu, L.-W. Fan, and Z.-T. Yu, "Determination on the Thermal Conductivity and Thermal Contact Resistance of Thin Composite Phase Change Films as a Thermal Interfacial Material," *Case Studies in Thermal Engineering* 33 (2022): 101979, https://doi.org/10.1016/j.csite.2022.101979.

52. Y. Cao, J. Su, Y. Xiao, et al., "Functional Biomass/Biological Macromolecular Phase Change Composites and Their Applications in different scenarios: a review," *International Journal of Biological Macromolecules* 306, no. Pt 3 (2025): 141377, https://doi.org/10.1016/j.ijbiomac.2025.141377.

53. W. Huo, Z. Xia, Y. Gao, R. Guo, and X. Huang, "Flexible Thermoelectric Devices With Flexible Heatsinks of Phase-Change Materials and Stretchable Interconnectors of Semi-Liquid Metals," *ACS Applied Materials & Interfaces* 15, no. 24 (2023): 29330–29340, https://doi.org/10.1021/acsami.3c05418.

54. Z.-M. Li, W. Liu, M.-Y. Liu, et al., "Liquid Metal-Based Flexible Heat Sink for Adaptive Thermal Management," *Applied Thermal Engineering* 256 (2024): 124071, https://doi.org/10.1016/j.applthermaleng.2024.124071.

55. H. Bark, M. W. M. Tan, G. Thangavel, and P. S. Lee, "Deformable High Loading Liquid Metal Nanoparticles Composites for Thermal Energy Management," *Advanced Energy Materials* 11, no. 35 (2021): 2101387, https://doi.org/10.1002/aenm.202101387.

56. X. Shan, S. Chen, W. Feng, et al., "Anisotropic 3D-Printed Carbon Fiber-Reinforced Liquid Metal Elastomer for Synergistic Enhancement of Electrical Conductivity, Thermal Performance, and Leakage Resistance," *Advanced Materials* 38, no. 3 (2026): 11498, https://doi.org/10.1002/adma.202511498.

57. M. J. Assael, A. Chatzimichailidis, K. D. Antoniadis, W. A. Wakeham, M. L. Huber, and H. Fukuyama, "Reference Correlations for the Thermal Conductivity of Liquid Copper, Gallium, Indium, Iron, Lead, Nickel and Tin," *High Temperatures-High Pressures* 46, no. 6 (2017): 391–416.

58. V. Y. Prokhorenko, V. V. Roshchupkin, M. A. Pokrasin, S. V. Prokhorenko, and V. V. Kotov, "Liquid Gallium: Potential Uses as a Heat-Transfer Agent," *High Temperature* 38, no. 6 (2000): 954–968, https://doi.org/10.1023/A:1004157827093.

59. L. Dejace, H. Chen, I. Furfaro, G. Schiavone, and S. P. Lacour, "Microscale Liquid Metal Conductors for Stretchable and Transparent Electronics," *Advanced Materials Technologies* 6, no. 11 (2021): 2100690, https://doi.org/10.1002/admt.202100690.

60. S. Chen, S. Li, Y. Li, P. Dong, and S. Yao, "Programming Magnetic Composites and Phase Change Materials for Multimodal Haptic Interfaces With Integrated Self-Sensing Toward Adaptive and Proprioceptive Haptic Feedback," *Materials Horizons* 13, no. 8 (2026): 4155–4169, https://doi.org/10.1039/D5MH01998B.

61. C. Hatzfeld and T. A. Kern, *Engineering Haptic Devices*, 2nd ed. (Springer, 2014).

62. S. Yao, P. Ren, R. Song, et al., “Nanomaterial-Enabled Flexible and Stretchable Sensing Systems: Processing, Integration, and Applications,” *Advanced Materials* 32, no. 15 (2020): 1902343, https://doi.org/10.1002/adma.201902343.

63. J.-H. Kim, A. Vázquez-Guardado, H. Luan, et al., “A Wirelessly Programmable, Skin-Integrated Thermo-Haptic Stimulator System for Virtual Reality,” *Proceedings of the National Academy of Sciences* 121, no. 22 (2024): 2404007121, https://doi.org/10.1073/pnas.2404007121.

64. Z. Wang, T. Zhang, B. K. Park, W. I. Lee, and D. J. Hwang, “Minimal Contact Formation Between Hollow Glass Microparticles Toward Low-Density and Thermally Insulating Composite Materials,” *Journal of Materials Science* 52, no. 11 (2017): 6726–6740, https://doi.org/10.1007/s10853-017-0908-x.

Supporting Information

Additional supporting information can be found online in the Supporting Information section.

Supporting File: smll75512-sup-0001-SuppMat.docx.